Author Manuscript

Wind and turbulence observations with the Mars microphone on Perseverance

Alexander E. Stott[1], Naomi Murdoch[1], Martin Gillier[1], Don Banfield[2], Tanguy Bertrand[3], Baptiste Chide[4], Manuel De la Torre Juarez[5], Ricardo Hueso[6], Ralph Lorenz[7], German Martinez[8,9], Asier Munguira[6], Luis Mora Sotomayor[10], Sara Navarro[10], Claire Newman[11], Paolo Pilleri[12], Jorge Pla-Garcia[10], Jose Antonio Rodriguez-Manfredi[10], Agustin Sanchez-Lavega[6], Michael Smith[13], Daniel Viudez Moreiras[10], Nathan Williams[5], Sylvestre Maurice[12], Roger C. Wiens[14], David Mimoun[1]

[1]Institut Supérieur de l'Aéronautique et de l'Espace (ISAE-SUPAERO), Université de Toulouse, Toulouse, France.
[2]NASA Ames, Mountain View, CA, USA
[3]Laboratoire d'Etudes Spatiales et d'Instrumentation en Astrophysique (LESIA), Observatoire de Paris-PSL, CNRS, Sorbonne Université, Université de Paris Cité, Meudon, France.
[4]Space and Planetary Exploration Team, Los Alamos National Laboratory, Los Alamos, NM, USA.
[5]Jet Propulsion Laboratory – California Institute of Technology, Pasadena, CA, USA.
[6]Fisica Aplicada, Escuela de Ingeniería de Bilbao, Universidad del País Vasco UPV/EHU, Bilbao, Spain.
[7]Johns Hopkins Applied Physics Lab, Laurel, MD, USA.
[8]Lunar and Planetary Institute, USRA, Houston, TX, USA.
[9]University of Michigan, Ann Arbor, MI, USA.
[10]Centro de Astrobiologia (CAB), CSIC-INTA, Madrid, Spain
[11]Aeolis Research, Chandler, AZ, USA.
[12]Institut de Recherche en Astrophysique et Planétologie (IRAP), Université de Toulouse 3 Paul Sabatier, CNRS, CNES, Toulouse, France.
[13]Goddard Space Flight Center, Greenbelt, MD, USA.
[14]Purdue University, West Lafayette, IN, USA.

Key Points:

- Wind-induced noise is observed by the SuperCam Mars microphone on Perseverance.
- Microphone and air temperature data are used to estimate the wind speed at high frequencies, using a machine learning model.
- The wind speed estimate is used to examine the relationships between turbulent intensity, pressure drops, temperature and energy flux.

Corresponding author: Alexander Stott, Alexander.stott@isae-supaero.fr

This is the author manuscript accepted for publication and has undergone full peer review but has not been through the copyediting, typesetting, pagination and proofreading process, which may lead to differences between this version and the Version of Record. Please cite this article as doi: 10.1029/2022JE007547.

This article is protected by copyright. All rights reserved.

Author Manuscript

Abstract

We utilise SuperCam's Mars microphone to provide information on wind speed and turbulence at high frequencies on Mars. To do so, we first demonstrate the sensitivity of the microphone signal level to wind speed, yielding a power law dependence. We then show the relationship between the microphone signal level and pressure, air and ground temperatures. A calibration function is constructed using Gaussian process regression (a machine learning technique) taking the microphone signal and air temperature as inputs to produce an estimate of the wind speed. This provides a high rate wind speed estimate on Mars, with a sample every 0.01 s. As a result, we determine the fast fluctuations of the wind at Jezero crater which highlights the nature of wind gusts over the martian day. To analyse the turbulent behaviour of this wind speed estimate, we calculate its normalised standard deviation, known as gustiness. To characterise the behaviour of this high frequency turbulent intensity at Jezero crater, correlations are shown between the evaluated gustiness statistic and pressure drop rates/sizes, temperature and energy fluxes. This has implications for future atmospheric models on Mars, taking into account turbulence at the finest scales.

Plain Language Summary

The NASA Perservance mission sent microphones to the surface of Mars. This microphone has recorded signals due to the wind. We examine how these recorded signals vary with other sensor data from Perseverance, which shows a link between the microphone signal, the dedicated wind speed sensor and air temperature. Based on this finding we develop a way to predict the wind speed from the microphone data using a machine learning technique. The microphone records data at a very high rate compared with sensors so far sent to Mars. This means that the wind speed predicted from the microphone data can be used to study the chaotic and variable wind behaviour on Mars to a level never seen before. We show that this chaotic and variable behaviour has links to temperature and the number of whirlwinds observed. This will lead us to better weather models for Mars.

1 Introduction

The NASA Perseverance mission searches for signs of past habitable environments in Jezero crater, part of an ancient delta on Mars (Farley et al., 2020; Mangold et al., 2021), as it also prepares for future human exploration. A large part of this search requires the determination of the dynamic processes currently at play on Mars (Dundas et al., 2021). One major contributor of day to day surface alteration is through aeolian processes, whereby dust and sand are lofted and transported. Such activity ranges from the movement of single particles and local dust lifting in dust devils, to larger scale dust lifting events by wind gusts and even dust storms which can become global (Zurek & Martin, 1993; Wang & Richardson, 2015; Newman et al., 2022; Charalambous, McClean, et al., 2021; Murdoch et al., 2022). The control and variation of these processes is yet to be fully understood, and so, in situ measurements of the dynamic atmospheric environment, particularly turbulence, can yield new insights.

Perseverance provides the first measurements of the Martian soundscape (Maurice et al., 2022; Mimoun et al., 2023). The current catalogue of recordings includes rover noises, the Ingenuity rotorcraft, shock waves from the SuperCam Laser Induced Breakdown spectroscopy (LIBS) technique and the noise of the Martian wind. The microphone has also recorded winds and saltation due to a passing dust devil (Murdoch et al., 2022). The propagation and origin of these sounds depend on the properties of the atmosphere and their variation. Notably, these measurements are at a high rate (up to 100 kHz but more usually 25 kHz) and, therefore, they offer a new way to observe the high frequency atmospheric variation on Mars. This high frequency sampling of atmospheric variations

This article is protected by copyright. All rights reserved.

Author Manuscript

is important to characterise stochastic variations in the Planetary Boundary Layer (PBL), in particular how the energy dissipates at the small scales (Maurice et al., 2022). This turbulent behaviour is linked to dust lifting and so its characterisation is important to understand the ongoing surface change on Mars (Dundas et al., 2021; Newman et al., 2022).

The aim of this work is to use the SuperCam microphone data to characterise the wind speed and its turbulent behaviour at high frequencies. To do so, we first provide a sensitivity analysis of the SuperCam microphone recordings to the properties of the ambient Martian atmosphere. The signal is shown to be correlated primarily to the wind speed with contributions from the variation in the wind speed (its standard deviation), temperature and pressure variation. We next use these sensitivities to produce a calibration of microphone and air temperature data to wind speed and so infer a wind speed estimate based on the microphone data. This is achieved though Gaussian process (GP) regression (Williams & Rasmussen, 1995), a machine learning technique. This wind speed estimate represents the highest frequency wind speed measurement obtained on Mars so far. We examine this estimate for a range of atmospheric conditions to show the different characteristics highlighted by the GP prediction. By calibrating the microphone and air temperature to a wind speed, we obtain a more straightforward to interpret signal in terms of existing wind analysis techniques. This is done here in terms of the gustiness metric, a marker of turbulent intensity. We then show how the calculated gustiness correlates with measured environmental data from the Perseverance meteorological sensor package (J. A. Rodriguez-Manfredi et al., 2021) to examine how turbulence in the PBL can be controlled. Moreover, we provide a comparison to pressure drop rates, another marker of convective activity/turbulence. As a result, we demonstrate how to use the microphone to extract information on turbulence at high frequencies, shedding light on the PBL dynamics.

2 The Martian Planetary boundary layer

The PBL is the part of the atmosphere at the interface with the planetary surface. This region represents the atmosphere directly affected by the surface and, on Mars, this is where heat, momentum, chemical species and dust are mixed with the free atmosphere (Petrosyan et al., 2011; Spiga, 2019). It is therefore, crucial to the overall climate modelling of Mars (Read et al., 2015, 2017).

The thin Martian atmosphere is inefficient at heating and cooling the surface and so during the day the PBL is forced by radiative flux with little conductive influence (Petrosyan et al., 2011; Spiga, 2019). Some models, however, suggest near surface heating (and drive for convection) by sensible and radiative effects to be roughly equal (Wu et al., 2021). This is because, although the radiative heat flux is greater at the surface, most passes through the lower atmosphere without being absorbed. In general, the warming of the surface generates large near surface temperature gradients causing instabilities and, thus, intense convective turbulence.

Convective vortices and even dust devils (dust loaded convective vortices) are a commonly observed feature on Mars (Balme & Greeley, 2006; Murphy et al., 2016; Lorenz et al., 2021; Kurgansky, 2019; Hueso et al., 2022b; Spiga et al., 2021). At the InSight landing site large pressure drops have been correlated to a few aeolian change events but with little dust lofting (Charalambous, McClean, et al., 2021). However, most other missions including Perseverance have seen many dust devils (Newman et al., 2022; Hueso et al., 2022b; Murdoch et al., 2022). On top of dust devils, convective cells have been observed to produce large dust lifting events at Perseverance which, although less frequent, likely contribute as significantly to overall aeolian transport (Newman et al., 2022; Viúdez-Moreiras, Torre, et al., 2022).

This article is protected by copyright. All rights reserved.

Author Manuscript

The Martian PBL grows throughout the daytime and can reach up to ∼10 km. At night, however, convective motions are inhibited by surface radiative cooling which leads to the collapse of the PBL and the formation of a near surface stable layer. At this time mechanical instabilities still occur (often influenced by topography i.e. slope winds) which generate shear turbulence. The effect on turbulence of wind shear is greatest near the surface as the wind speed generally follows a logarithmic profile with height (Monin et al., 2013), falling towards zero at the surface. Chatain et al. (2021) demonstrated the evolution of turbulence over the seasons at InSight, where shear driven turbulence was shown to be heavily prevalent during the winter and less so in summer. These features are also highly visible in the seismic data recorded by InSight where each type of turbulence exhibits a distinctive signature in the seismic noise (Charalambous, Stott, et al., 2021; A. Stott et al., 2023). Moreover, the ability for InSight to observe marsquakes is heavily modified by the seasonal evolution of turbulence.

These features of turbulence are prevalent in observed wind speed records. The Viking missions provided the first in situ records of wind speed on Mars (Hess et al., 1977; Gómez-Elvira et al., 2014). Further data sets have been acquired by the Curiosity (Gómez-Elvira et al., 2012), InSight (Banfield et al., 2019, 2020) and Perseverance missions (J. Rodriguez-Manfredi et al., 2023; Newman et al., 2022). The Viking missions provides hourly averaged wind data for 1000 sols with some more complete periods of observation. On the other hand, Curiosity suffered damage on its sensing boards upon landing and recorded wind data using the surviving boards with reduced quality till sol 1491, when more boards were damaged, and no further data retrieval was possible (Viúdez-Moreiras et al., 2019b, 2019a). InSight has collected wind data for over a thousand sols with an almost continuous 1 Hz sampling of the first martian year of observations. The second Martian year, however, is sparsely recorded owing to power constraints. Analysis of these wind data have proven fruitful for the understanding of turbulence in the PBL. For example, Spiga et al. (2021) demonstrated a correlation between ground temperature and turbulent intensity (gustiness) to characterise the radiative control of the boundary layer. The Perseverance wind speeds were collected on a one hour on one hour off cadence and can be up to 2 Hz. Viúdez-Moreiras, Lemmon, et al. (2022); Viúdez-Moreiras, Torre, et al. (2022) has demonstrated that the winds at Jezero are generally calmer than other landing sites, but have a slightly higher turbulent intensity than at InSight. However, several boards of the Perseverance wind sensor were damaged (Viúdez-Moreiras, Lemmon, et al., 2022; Lemmon et al., 2022) due to wind-induced sand particle impacts especially during a regional dust storm on sols 313 and 315 (Hueso et al., 2022b), thus hindering the wind retrieval with the same accuracy. Continued data retrieval requires ongoing wind sensor re-calibration activities.

The turbulent wind flow is described as a distribution of eddies (Stull, 1988). In three dimensional fluids the turbulent energy enters the atmosphere at a source scale and generally causes eddies which continuously deconstruct into smaller eddies at the inertial scale. Finally, these eddies dissipate at scales when the viscous forces acting between the particles dominate. We can express this in terms of the PSD (power spectral density) of the turbulent wind flow. At the largest source region scales, which corresponds to the lowest frequencies below a few Hertz, the distribution is uniform with frequencies and so the PSD has no frequency dependence. In the inertial regime, where the eddies begin to deconstruct, the PSD decreases according to a power law. This power law is is usually given by Kolmogorov's law as $f^{-\frac{5}{3}}$, validated through experiments on Earth e.g. (Kaimal et al., 1972). Finally, in the dissipative regime, the PSD drops off very steeply with frequency as the distribution of eddies ceases.

In situ measurements on Mars do not always validate Kolmogorov's law ($f^{-\frac{5}{3}}$ for wind and $f^{-\frac{7}{3}}$ for pressure). The InSight pressure data demonstrated a shallower slope that expected for the inertial regime (Banfield et al., 2020; Temel et al., 2022). For Perseverance at Jezero, Viúdez-Moreiras, Torre, et al. (2022) demonstrated a slightly shal-

This article is protected by copyright. All rights reserved.

Author Manuscript

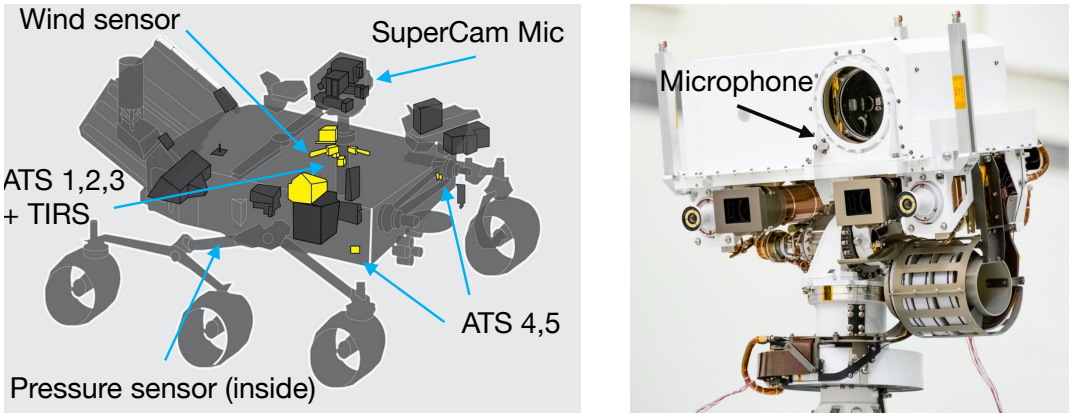


Figure 1. Left: Diagram of the Perseverance rover with the locations of instruments used highlighted. Right: Picture of the mast head housing the SuperCam instrument with the microphone location indicated. Credits NASA/JPL-Caltech for the right image, adapted from (Mimoun et al., 2023; Maurice et al., 2021).

lower than $f^{-\frac{5}{3}}$ slope for winds (below 0.5 Hz) and De la Torre Juárez and et al. (2022) showed steeper slopes (-2.6 and -1.9 between 0.1-1 Hz) for temperature. Of particular note, on Mars the dissipative regime begins at lower frequencies than on Earth. The Kolmogorov lengthscale for Mars is given as $\eta_s \approx 0.02$ m rather than the $\eta_s = 0.001$ m often used for Earth. Maurice et al. (2022) demonstrated this with the Mars microphone, showing an $\sim f^{-5}$ power law for frequencies above a few Hertz.

3 The sensors on Perseverance

3.1 Microphone recordings

Perseverance carries two microphones, one in the SuperCam instrument suite (Mimoun et al., 2023; Maurice et al., 2021) mounted on top of the remote sensing mast head 2.1 m above the ground, which can be rotated 360 degrees/pitched up and down. Figure 1 shows the location of the SuperCam microphone on the Perseverance rover mast head. The external dimensions of the mast head housing the SuperCam instrument are 480 mm by 260 mm by 180 mm, with the microphone protruding by 27 mm. Another microphone intended to listen to the entry descent and landing, referred to as the EDL microphone, is bolted to the rover body at 1 m height on the port side (Maki et al., 2020). In this work we only use data from the SuperCam microphone as its calibration is well characterised (Mimoun et al., 2023).

Here we specifically exploit the passive microphone recordings of the martian atmosphere, where the microphone records purely the ambient sound with no simultaneous rover operations. Such recordings are typically sampled at 25 kHz and last for 167 s. The wind-related signal itself is below 1 kHz (Maurice et al., 2022; Mimoun et al., 2023). The microphone also records the shock-waves from the LIBS shots in order to examine the properties of the rock (Murdoch et al., 2019; Chide et al., 2019, 2020). For LIBS, the microphone records at a sampling rate of 100 kHz as the acoustic signal ranges typically from 2 kHz to 20 kHz.

An operational campaign was constructed to perform around eight 167s long (the longest possible continuous recording (Mimoun et al., 2023)) recordings at 25 kHz every month. The aim was to extract the variation over the Martian sol but timings varied, for example, to prioritise day time signals (to ensure high signal to noise ratio record-

This article is protected by copyright. All rights reserved.

Author Manuscript

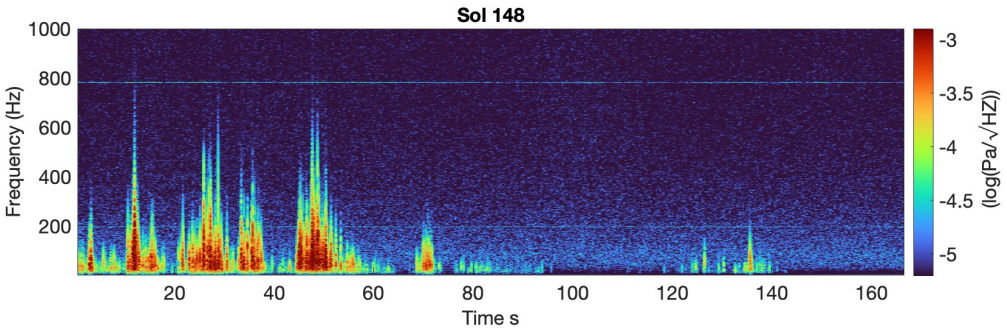


Figure 2. A spectrogram of a microphone recording taken on sol 148.

ings) or due to operational constraints. Another series of recordings were taken during the "360 degree spin" calibration activity. This activity took 30s long microphone recordings at different stopping angles while the SuperCam mast head was rotated through 360 degrees in order to improve the likelihood of finding any directional impact on the wind sensitivity. The general passive recordings were obtained over a range of mast and rover yaws.

The data selected cover Ls (solar longitude) 10-260 degrees which correspond to the Perseverance mission sols 0-483. The raw SuperCam microphone data are available in Wiens and Maurice (2021). Figure 2 shows a spectrogram of an example recording on sol 148 with large wind gusts exciting frequencies up to 800 Hz. As mentioned, the wind rarely generates signal above 1 kHz and so this is the upper bound of frequencies we will examine in this work. On the other hand, the lower frequencies show stronger intensity (darker red) than the higher frequencies indicating that the lower frequency content dominates the wind-induced signal. At the lower limit, we examine signals down to 20 Hz as below this it is not well calibrated. For in depth details of the microphone and its calibration/installation see Mimoun et al. (2023).

3.2 Atmospheric instruments and data

Perseverance carries the Mars Environmental Dynamics Analyser (MEDA) sensor package to measure the wind, air/surface temperatures and pressure, among other atmospheric variables, on Mars (J. A. Rodriguez-Manfredi et al., 2021). The raw data from the MEDA package are available (J. A. Rodriguez-Manfredi & de la Torre Juarez, 2021). Figure 1 shows the relative location of each sensor on the rover. MEDA measures complete even/odd hours in even-/odd- numbered sols including five minutes at the start of each hour, resulting in full coverage of the diurnal cycle every 2 sols. The wind sensor consists of two booms located 1.5m above the ground and separated by 120 degrees. Each boom provides independent measurements of wind speed and direction. Depending on the wind direction (which affects whether rover elements block the flow of the wind to one particular boom) one boom is selected to give the derived winds for a given period. The best of the two measurements is determined by a specific algorithm calibrated on wind tunnel experiments (J. A. Rodriguez-Manfredi et al., 2021). The wind speed retrieval has a resolution of ± 0.5 m/s and accuracy of 1 m/s up to 10 m/s and resolution and accuracy of 10% of the wind speed above this. The wind direction retrieval has an accuracy of $\pm$ 15 degrees. The wind speed data is usually sampled at a rate of 1 Hz.

The pressure sensor (PS) is based on the silicon-micro-machined pressure sensor head (Barocap) and transducer technology developed by Vaisala Inc. (J. A. Rodriguez-

This article is protected by copyright. All rights reserved.

Author Manuscript

Manfredi et al., 2021; Sánchez-Lavega et al., 2022). The MEDA PS is located inside the rover body with an inlet that connects the sensor with the exterior. The pressure is measured with a sampling rate of 1 Hz.

Three atmospheric temperature sensors (ATS 1, 2 and 3) are located on the remote sensing mast at a height of 1.45m and a further two (ATS 4 and 5) are located on the front of the rover at a height of 0.85m (J. A. Rodriguez-Manfredi et al., 2021). The recording of temperature fluctuations on these sensors depends on the direction from which the air parcel comes from and also the influence of the rover. Each sensor records at up to 2 Hz (more usually taken at 1 Hz) and they have a response time to temperatures at 0.5s for wind speeds above 5 m/s while they have a response of 0.77s to temperatures at 0 m/s. Details of the air temperature dataset are covered in Munguira et al. (2023).

Ground temperature and atmospheric downwelling Infrared (IR) flux values are obtained from the Thermal Infrared Sensor (TIRS) (Smith et al., 2023; Sebastián et al., 2020, 2021) with the latter available in (Smith, 2022). The data recorded by the MEDA sensors enable the estimation of turbulent (sensible) heat flux. The values used in this paper are retrieved through similarity theory in Martínez et al. (2022) and available in Martinez (2022).

4 The sensitivity of the SuperCam microphone to atmospheric data

4.1 Microphone wind noise

Wind noise is a known phenomena on microphone recordings and signals can be generated by several mechanisms (for a summary see e.g. Lyons et al. (2021)). Microphones are usually used to record sound waves and a turbulent parcel of wind can itself generate sound waves (Lighthill, 1954). However, this is not often the means by which wind generates signals on microphones. The more dominant effect is due to pressure fluctuations and not sound waves. Such pressure fluctuations arise from the stagnation pressure, that is, the pressure at the surface of a body placed in a wind flow (Raspet et al., 2006). The pressure fluctuations arise from Bernoulli's principle and are given as

$$p(t) = \frac{1}{2}\rho V(t)^2 \tag{1}$$

where ρ is the air density and $V(t)$ is the velocity of the wind flow. The wind velocity in the PBL is usually decomposed as

$$V(t) = u(t) + U \tag{2}$$

where U is the mean speed of the wind flow and $u(t)$ accounts for the turbulent fluctuations of the wind flow (Monin et al., 2013). The pressure fluctuations are then expanded as $p(t) = \frac{1}{2}\rho(U^2 + u(t)^2 + 2u(t)U)$. In outdoor recordings, the pressure fluctuations recorded by a microphone can often be approximated as

$$p(t) \approx \rho u(t) U. \tag{3}$$

This was demonstrated by Morgan and Raspet (1992) who showed that the microphone signal level was better correlated to the product of the mean wind speed and root mean square (RMS) wind fluctuations than to either factor independently.

The approximation in equation (3) is used as the basis for the wind noise models of Raspet et al. (2006) and Van den Berg (2006). These models show that the microphone signal is therefore dependent on the turbulent flow of the wind, $u(t)$, in the PBL. Raspet et al. (2006) and Van den Berg (2006) demonstrate that Kolmogorov's "law of -5/3" is a good prediction for microphone wind noise. The fit to an $f^{-\frac{5}{3}}$ spectra is particularly good for unscreened microphones (Raspet et al., 2006, 2008), as is the case for

This article is protected by copyright. All rights reserved.

Author Manuscript

the SuperCam microphone. The identification of such a $f^{-\frac{5}{3}}$ slope has been used for automatic wind noise detection and reduction (Cook et al., 2021).

In certain circumstances, however, microphones can observe intrinsic pressure fluctuations (Raspet et al., 2006). In this case spectra in the inertial range drop off as $f^{-\frac{7}{3}}$. Matching -7/3 slopes have been observed in experiments such as Wilson et al. (2007) and Hart et al. (2018). The mean wind shear flow can also interact with turbulent fluctuations which generates an effect seen usually only at very low frequencies, below those examined here (Raspet et al., 2008).

Van den Berg (2006) also introduces an extra f^{-2} slope due to a low-pass filter effect of a wind screen. This occurs for frequencies where the lengthscale of the turbulent eddies is small enough to average out over the wind screen surface. Wilson et al. (2007) observes the same effect for slopes consistent with intrinsic pressure fluctuations ($f^{-\frac{7}{3}}$), as well as from the stagnation pressure ($f^{-\frac{5}{3}}$).

Van den Berg (2006) also calculates the sensitivity of the signal level to the mean wind speed. This is shown to be dependent on the frequency slope of the turbulent fluctuations. For frequencies in the inertial regime below the low-pass filter effect noted above, the signal level varies as $46.67\log(U)$, which is in the range of the U^2-U^3 observed in experimental data by Morgan and Raspet (1992). For frequencies above the low-pass filter corner frequency, Van den Berg (2006) shows that the microphone signal level is proportional to $66.67\log(U)$, that is, a $U^{3.33}$ sensitivity.

4.2 Wind noise on the SuperCam microphone

Here, we demonstrate the sensitivity of the SuperCam microphone signal level to the wind speed measurements on Mars. The signal level is given as the microphone sound pressure level (SPL), calculated as

$$SPL = \log_{10}\left(\frac{\mathbf{p}}{p_{ref}}\right) \tag{4}$$

where $\mathbf{p}$ is the RMS pressure of the microphone pressure signal and $p_{ref} = 20\mu$Pa is a reference pressure.

Figure 3 (a) and (b) shows the relationship between the mean wind speed and the microphone SPL in the 20-60 Hz and 100-1000 Hz frequency bands respectively. The relationship between wind speed and the SPL in the 20-60 Hz bandwidth can be approximated by a U^4 power law above a threshold. The SPL in the 100-1000 Hz range is more sensitive to wind, with a much steeper rise following a threshold. A power law fit is not well constrained here. The threshold increases with frequency as ~ 2 m/s for the SPL in the 20-60 Hz range whereas it is ~ 4 m/s for the 100-1000 Hz range. The colour of the dots representing each recording correspond to the time of sol. This demonstrates the recordings below the threshold are typically darker colours during the night or outside the main daytime convective period. There is some structure to this threshold as some recordings below it do exhibit some signal and several recordings above it do not show much signal.

These bandwidths represent the frequency limits we can examine as the microphone is not well calibrated below 20 Hz and wind-induced signals are rarely seen above 1 kHz, as demonstrated by the increasing threshold with frequency. We select the 20-60 Hz bandwidth for use in the rest of this paper as it contains the most wind-induced signal and the relationship is more clearly defined.

The correlations in Figure 3 establish a relationship between the wind speed and the microphone signal. This relationship can be considered as an in situ calibration of the microphone data to the wind speed. The demonstrated U^4 relationship is close to the $U^{3.33}$ factor derived by Van den Berg (2006) for frequencies above the wind screen

This article is protected by copyright. All rights reserved.

Author Manuscript

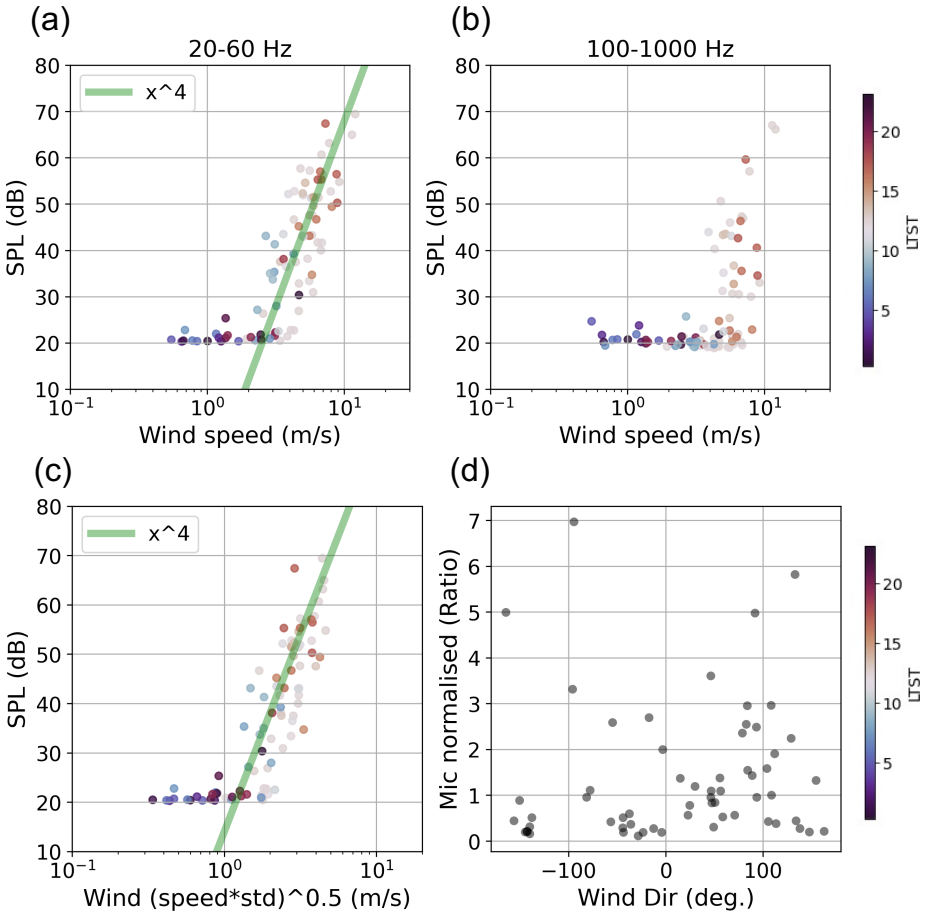


Figure 3. Scatter plots of the microphone SPL against the mean wind speeds (from MEDA) in 20-60 Hz (a) 100-1000 Hz (b) frequency bands with a power law approximation shown in green. (c) Scatter plot of the microphone SPL in the 20-60 Hz frequency band against the product of mean and standard deviation of the wind speed (from MEDA). For (a)-(c), each dot represents a 167 s (or 30 s from the 360 turn) microphone recording and the colour of the dot represents the Local True Solar Time (LTST) of the recording. (d) Incident wind direction to the microphone against the Mic RMS pressure normalised by the power law approximation in (a) for only 167s microphone recordings with a wind speed > 3 m/s.

This article is protected by copyright. All rights reserved.

Author Manuscript

low-pass filter effect. As, according to Van den Berg (2006), the sensitivity to wind depends on the turbulence spectral slope, the slight discrepancy could be explained by the nature of the frequency spectra observed on Mars compared to Earth, outlined above. In particular, recall that the dissipative regime begins at lower frequencies on Mars and has a steeper slope than the inertial regime.

Figure 3 (c) shows the correlation of the SuperCam microphone SPL (20-60 Hz) with the product of the mean and standard deviation of the MEDA wind speed. As introduced above, Morgan and Raspet (1992) showed this to have superior correlation than to the mean wind speed. Here, we do not see a significant difference. This is likely due to the shorter time averages. Moreover, the standard deviation is calculated below 0.5 Hz as this is the limit of the MEDA data.

Prior to launch, Chide et al. (2021) tested the SuperCam microphone in a wind tunnel under Martian analogue conditions (low pressure CO_2) to verify its performance, using the same installation as on Mars. This experiment determined a generally quadratic relationship between the wind speed and the microphone RMS pressure in the 100-500 Hz range, where we see a lower sensitivity on Mars. This does not match the observed sensitivity on Mars and so we do not apply the calibration of Chide et al. (2021) to the Mars data. This difference could be explained by a consideration of the turbulent environment of the pre-mission testing. As noted in Morgan and Raspet (1992) and Van den Berg (2006), wind tunnel flows are less turbulent than outdoor atmospheric flows. In low turbulence flows the wind noise will be generated by the turbulence produced from the microphone housing (wake) rather than interactions with the atmospheric turbulent flow. Strasberg (1988) performed a dimensional analysis of data collected from moving microphones with a spherical or cylindrical windscreen through the air in a lab, a very low atmospheric turbulence case. A dimensional analysis of this data showed that the normalised (dimensionless) sound pressure level collapses to a single curve in terms of dimensionless frequency (Strouhal number = $\frac{fD}{U}$, where D is the diameter of the windscreen). Raspet et al. (2006) indicates that this scaling law represents a self-noise limit for wind noise reduction on a non-streamlined windscreen. Hart et al. (2018) produced a dimensional analysis similar to Strasberg (1988) for outdoor data and notes the difference in mechanics for the outdoor turbulence results in an alternative relationship to that given by Strasberg (1988).

Chide et al. (2021) also found the wind incident direction contributed up to a factor of 2 difference in RMS pressure, consistent with the effect of wake turbulence. This sensitivity to wind direction was more pronounced at higher frequencies (above 500 Hz). To investigate any effect of wind incidence direction on Mars, Figure 3 (d) shows the ratio of the SPL in the 20-60 Hz frequency band to a U^4 fit. No clear relationship with a particular direction is apparent, as is also the case for higher frequencies which were seen to be more sensitive to this effect in the pre-mission testing on Earth in Chide et al. (2021). Therefore, although the pre-flight characterisation tests were valuable to demonstrate that the SuperCam microphone would be sensitive to wind in Martian analogue conditions, the behaviour of the wind noise observed in Chide et al. (2021) does not match the observed data on Mars in terms of sensitivity to wind speed or direction. To that end, we use the observed, in situ, relationships presented here to interpret the Mars dataset. As described, this difference is consistent with the fact that the wind tunnel data are in a less turbulent environment meaning the mechanics for wind noise generation may be different.

4.3 The co-variation of microphone SPL and atmospheric signals

The primary source of signal level on the microphone is from the wind speed, summarised by the power law relationship with the mean wind speed as shown in Figure 3. However, there is a statistical spread/scatter. This is in part due to the relatively short

This article is protected by copyright. All rights reserved.

Author Manuscript

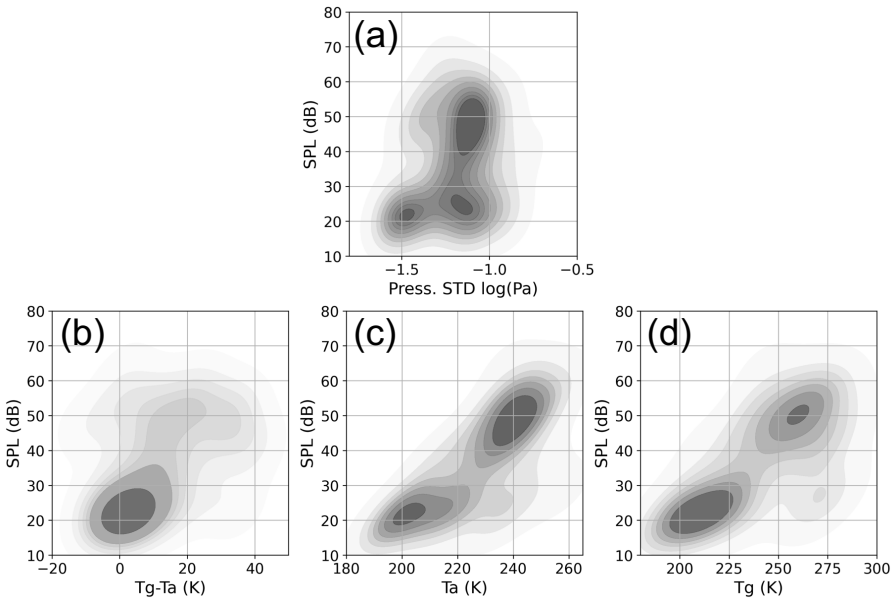


Figure 4. Kernel density estimates (KDE) of the two-dimensional histograms for the microphone SPL in the 20-60 Hz frequency band against (a) pressure standard deviation (b) the difference between ground temperature, Tg, and air temperature, Ta, (c) air temperature Ta and (d) ground temperature Tg.

time averages in our data, as our recordings can only be taken over 167 s. We can also look to other data to help describe the microphone signal. To that end, we will explore the relationship between the microphone SPL and other meteorological measurements from the MEDA suite.

Figure 4 (a) shows the correlation between the standard deviation of the pressure (from the MEDA sensor sampled at 1 Hz) and the microphone SPL in the form of a two-dimensional probability density function (PDF), i.e. the joint distribution. The PDF is estimated using kernel density estimation (KDE), which is a kernel smoothing applied to a histogram. This relationship demonstrates the impact of pressure fluctuations. The standard deviation of pressure has been shown to be correlated to wind speed in Charalambous, Stott, et al. (2021) for InSight, and so provides complementary information. There is a generally positive relationship between the two, although there is a density of recordings which don't correlate as well. This mirrors the threshold effect shown in Figure 3.

The colour coding of Figure 3 indicates the time of Sol. This indicates the times of day likely to see such signal level on the microphone. For example, it can be seen that the higher wind speeds and microphone SPL correspond to the middle of the sol during the convective period. These lighter coloured points, however, have a wide range of values indicating that high a SPL is not always the case for recordings near midday. The points which don't correlate to wind speed, on the other hand, are typically at nighttime or late morning suggesting they are either for a more stable atmosphere (less turbulent flows which the microphone is less sensitive to) or where we observe a lull.

To further investigate this structure, we consider the variation of the microphone SPL with air temperature (Ta), ground temperature (Tg) and the temperature difference between air and ground (Tg-Ta) in Figure 4, which shows the joint distributions with each variable. These variables share a forcing mechanism and are, in turn, correlated to each other. The thermal gradient, Tg-Ta, is the generative mechanism for con-

This article is protected by copyright. All rights reserved.

Author Manuscript

vective turbulent winds, the predominant source of daytime turbulence. This is demonstrated for Perseverance in De la Torre Juárez and et al. (2022); Munguira et al. (2023), where the air temperature fluctuations (due to turbulence) are shown to be correlated to the temperature gradient. However, the relationship between the SPL and air temperature is the most consistent in Figure 4. The superior correlation with air temperature may be due to the faster response time of the ATS sensors. On the other hand, the ground temperature data does not fluctuate on such fast scales and its value depends on the surface thermal inertia and albedo, which change as the rover moves (Martínez et al., 2022). Moreover, the impact of ground temperature on the thermal gradient would be an average over the terrain in terms of effecting the wind field.

The temperature can be used to indicate diurnal variations in terms of atmospheric stability. Temel et al. (2022) demonstrated a range of Martian pressure spectra for time periods where turbulence would be driven by different mechanisms. Van den Berg (2006) and Hart et al. (2018) have shown that the atmospheric stability plays a part in the turbulent spectrum observed by a microphone. As a result, the temperature data is helpful to describe the microphone SPL and the wind speed.

We note that one other possible source of this statistical scatter could be due to vertical winds, which would produce signal on the microphone in the same way. As the microphone data do not show much dependence on the wind incidence direction, the microphone is likely equally sensitive to such vertical winds. Vertical wind speeds are generally lower than horizontal (0.2 of the size of horizontal wind speed is used as a rule of thumb (Lorenz, 2022)) and are often correlated to horizontal winds. Chide et al. (2022) demonstrate an analysis of thermal fluctuations based on sound speed measurements from recordings of the LIBS shockwave. This indicated the presence of significant, fast thermal fluctuations, both vertical and horizontal, at Jezero. The MEDA wind sensor currently only determines horizontal wind speeds. These are isolated from vertical wind contributions, although separate vertical wind retrievals have not yet been obtained.

5 Wind speed estimation with Gaussian process regression

The goal now is to produce a wind speed estimator based on the microphone signal. Such an estimator allows us to make use of the high frequency wind information provided by the microphone. By converting to wind speed it is more straightforward to interpret in a meteorological sense. Furthermore, it demonstrates the use of microphones as wind speed sensors in planetary missions. As the MEDA wind sensor suffered damage due to grain impacts (Viúdez-Moreiras, Lemmon, et al., 2022), this is of use to the Perseverance mission.

In order to produce such a prediction of wind speed, a calibration function must be obtained. Figure 3 (a) demonstrated a fourth order power law approximation between the microphone SPL and wind speed. However, there is considerable statistical spread/scatter. Although both the air and ground temperature are important to explain the physical processes in generating winds/turbulence, we choose to use the air temperature as it demonstrated the most consistent relationship owing to its faster response time. Moreover, there is a correlation between them and so some information is shared. This air temperature can therefore help take into account variations in the relationship based on the diurnal variation. To that end, we use both the microphone RMS pressure and air temperature data as inputs to a calibration model for the prediction of the wind speed.

5.1 Gaussian process regression for a calibration function

Supervised machine learning techniques represent a good choice for such curve fitting problems. In this application we desire a smooth calibration function so as to propagate the signal properties of the microphone data rather than find the best fitting per-

This article is protected by copyright. All rights reserved.

Author Manuscript

formance. This is because the MEDA wind sensor has its own calibration grid and we do not want to directly fit this but rather examine the different qualities/abilities from each of the respective sensors. On top of this, powerful fitting methods such as neural networks typically require several thousand data points as a minimum. As a result, we choose to implement Gaussian process (GP) regression for the task. We present a brief introduction to GP regression here and refer the reader to Williams and Rasmussen (1995) for a full review.

Gaussian processes are non-parametric, that is, they are not constrained to a functional form such as a power law. As a result, the calibration function does not suffer from artifacts due to an arbitrary construction. Instead a GP regression finds a distribution of potential functions which would fit the data as

$$\mathbf{f} \sim \mathcal{N}(\mathbf{m}, \mathbf{K}) \tag{5}$$

where $\mathbf{f}$ represents a vector of outputs of the function which is normally distributed in terms of the mean function $\mathbf{m}$ (specified as a vector and often set to zero following data normalisation) and $\mathbf{K}$ which is the covariance matrix of the data.

The covariance matrix is calculated based on a kernel function, evaluated for a given input sample x with another sample x' as $k(x, x')$, where the matrix $\mathbf{K}$ consists of values of $k(x, x')$ for several input samples X. The kernel function dictates the properties (e.g. smoothness) of the potential functions which can fit the data and are designed to give a valid covariance matrix for a normal distribution as above. One such kernel function (see Williams and Rasmussen (1995) for a variety of kernel choices) is the radial basis function (RBF) given by

$$k(x, x') = \sigma^2 \exp\left(-\frac{\|x - x'\|^2}{2l^2}\right)$$

where σ and l are the variance and characteristic lengthscale. These are termed hyperparameters and determine the variance and smoothness for functions dependent on the distance between inputs x and x'. These hyperparameters are optimised (through a process known as marginalisation, see Williams and Rasmussen (1995)) for a given set of training data. In our case the multivariate input, denoted X, is the microphone RMS pressure and air temperature and the output/target, denoted $\mathbf{y}$, is the corresponding observed wind speed.

The trained GP model represents a posterior distribution of functions $\mathbf{f}$ (in equation (5)) given the training data as $\mathbf{f}|X, \mathbf{y}$. To obtain a prediction for a set of new previously unseen inputs X^* we must infer from the conditional distribution $\mathbf{f}|X, \mathbf{y}, X^*$. The expected (mean) value of the distribution is taken as the prediction/estimate but distribution also yields the variance, leading to a quantification of the uncertainty of a predicted output for a new data point. In this way, the GP regression acts to interpolate the training data to provide predictions.

For our application, we trained a GP model using the GPy package (GPy, since 2012) in Python. The microphone RMS pressure and the MEDA air temperature were chosen as inputs while the MEDA wind speed represents the output for training. An RBF was chosen as a kernel function with independent lengthscales for the microphone RMS pressure and air temperature. The training data were the average values from 80% (68) of the total number (86) of 167s recordings taken with wind speed data available. The 80% was selected by taking recordings with a wind speed along an evenly spaced grid over the range of values. Two further representative samples were added from 1 s period within recordings with higher wind speeds (up to 13.3 m/s) as the averaged values did not allow for a calibration at this level. These training data were used to optimise the hyperparameters. The remaining 18 (20%) were used as test data to verify the fit for unseen data and ensure there is no overfitting. The trained GP model prediction for

This article is protected by copyright. All rights reserved.

Author Manuscript

both the training and test data had a root mean square error of 1.3 m/s. The wind speed estimates generated from the microphone and air temperature data are available A. E. Stott (2023).

5.2 Wind speed estimates analysis

The GP model trained above was used to produce wind speed estimates over the available microphone recordings. To that end, the running RMS pressure envelope was calculated for each microphone recording as a continuous input. The RMS pressure was calculated for the microphone signal over 1 s windows with an overlap of 99% between each successive window. This represents a sample every 0.01 s and the ATS data were interpolated to match. This yields high frequency wind speed signals over each 167 s length recording.

Figure 5 (a) and (b) shows two example wind speed estimates from the GP model. The top panel of each sub figure shows the wind speed retrieval from the MEDA sensor over that period in blue and the GP prediction based on the microphone data in black with the 95% confidence interval in shaded blue. In order to show the inputs for the GP model prediction the second and third panels shows the raw microphone RMS pressure envelope and the ATS sensor data respectively. The lowest value of the air temperature over the recording is taken as the input, indicated in black. In both recordings this is predominantly from ATS 1.

The first recording in Figure 5 (a) is taken around noon LTST when the surface to air thermal gradient is highest and at the height of convective activity. On the other hand, the second recording Figure 5 (b) is taken late in the afternoon after 1700 LTST just before the PBL collapses to show a contrast in conditions (Munguira et al., 2023). In both cases there is a good agreement between the microphone-based estimate and the MEDA wind speed which is almost always within the 95% confidence interval of the prediction for each example. In contrast, however, the microphone-based recordings generally exhibit sharper variations than the MEDA retrievals.

The noon recording in Figure 5 (a) shows episodic high speed gusts and low/steady wind speed lulls. The microphone shows gusts ranging from 1-10 s in length and with wind speed peaks above 10 m/s and the confidence interval upper bound up to 14 m/s. The MEDA wind speed retrieval also shows gusts but the lengths are all of the order of 10s with slightly lower peak wind speeds. During the low wind speed lulls the microphone estimate does not vary much, while the MEDA wind speed retrieval shows a slow change in wind speed magnitude. In this case, the wind variability is not enough to generate a signal on the microphone. This demonstrates the microphones lack of sensitivity to low or steady winds (also shown in Figure 3 (a)) as the energy in the wind shifts to lower frequencies. The air temperature helps provide information on this average wind level in such cases, accounting for information on the diurnal variation. As it is around midday, the air temperature is reasonably high and so the expected wind speed is relatively high. Wind speed predictions during the night, for example, show a lower average level with 0 m/s encompassed by the lower confidence interval.

The later afternoon recording in Figure 5 (b) has more persistent fluctuating winds, where the MEDA wind speed is always between 5-9 m/s. The microphone-based wind speed indicates a similar wind level but shows greater variability than the MEDA wind speed with shorter, sharper gusts of the order of seconds. Compared to the noon recording, however, there are no episodic gusts and the wind is fluctuating similarly all the time. The episodic gusts (mostly occurring before 80 s) in Figure 5 (a) are wider (of the order of $\sim$10 s, i.e. at 50 s) and there is a relatively long lull with little fluctuation after around 80 s into the recording. The air temperature for the afternoon recording is seen to be almost constant in comparison to the air temperature at noon which shows more

This article is protected by copyright. All rights reserved.

Author Manuscript

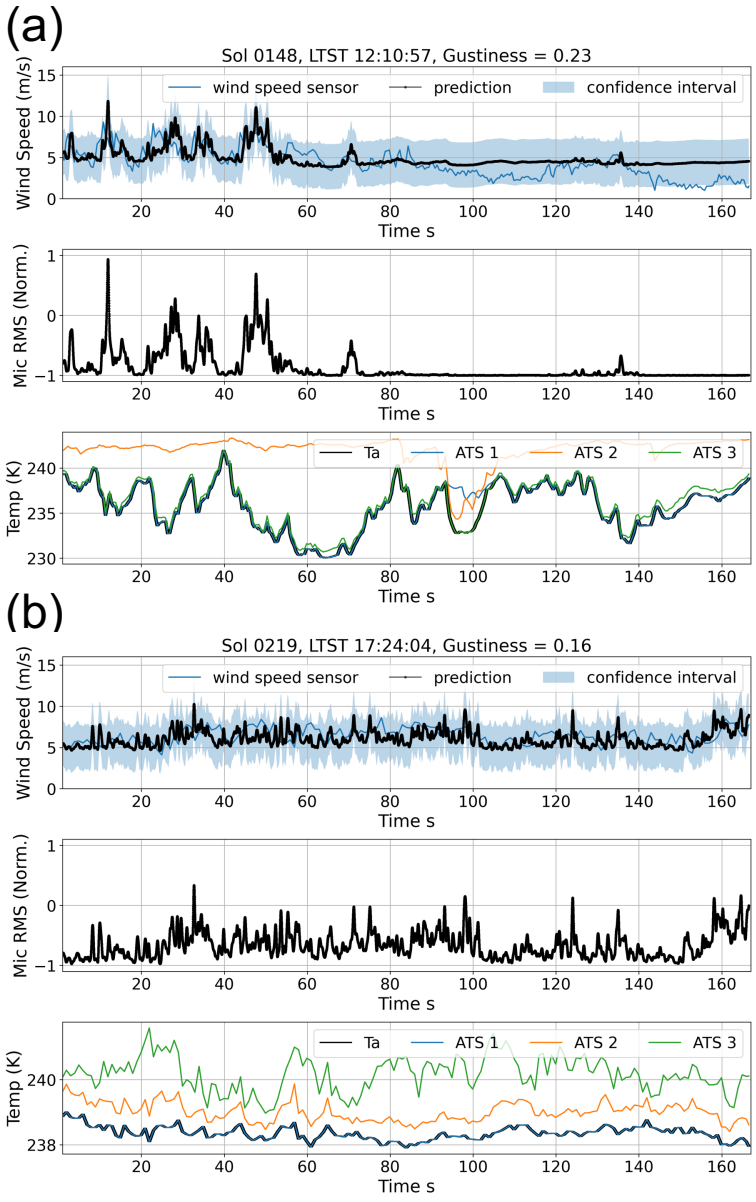


Figure 5. Wind speed estimates from the microphone and atmospheric temperature for two different recordings on sol 148 (Ls = 75) at 1210 LTST (a) and sol 219 (Ls = 107) at 1724 LTST (b). The former (a) is at the time of the largest ground to air thermal gradient with a developed PBL and the latter (b) is at the end of the afternoon just before the PBL collapse. The top panel shows the wind speed measured by MEDA (blue), the mean prediction from the GP (black) and the 95% confidence interval of the GP prediction shaded in blue. The second panel shows the RMS pressure of the microphone signal over the recording and the bottom panel shows the raw data from ATS 1, 2 and 3, where the minimum value (highlighted in black) over the recording is used as the input to the model.

This article is protected by copyright. All rights reserved.

Author Manuscript

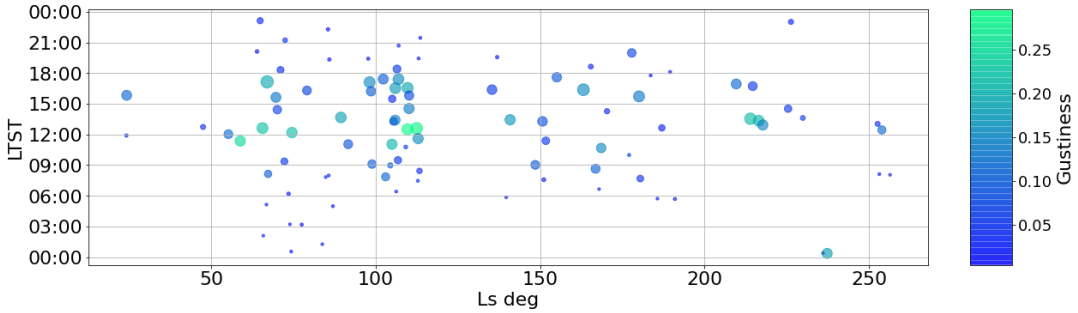


Figure 6. Microphone signal power and wind speed estimate gustiness over the mission. Each dot represents a 167s microphone recording where the size of the dot is scaled according to the RMS pressure of the recording and the colour indicates the gustiness metric for that recording.

significant fluctuation, demonstrated by the bottom panels of Figure 5 (a) and (b) respectively.

The microphone-based estimates, therefore, are reasonable wind speed retrievals, particularly for turbulent winds. The comparison to the MEDA wind speed retrievals shows that the microphone is able to resolve short, sharp wind gusts. These gusts have a greater degree of variability than captured by MEDA, with some showing higher wind speeds for shorter periods. This helps distinguish the different qualities of the signals at noon and late afternoon shown in Figure 5, where at noon there are clear episodic gusts and lulls and late afternoon fluctuates more consistently. On the other hand, the microphone is less suitable to study low level average wind speeds. The overall level of the GP model prediction does reasonably match the MEDA wind speed but it is not able to follow the low level variation. This is taken into account by the GP calibration as indicated by the wide range of the confidence intervals at low wind speeds.

6 PBL turbulence with microphone wind speed estimates

As shown in Figure 5, the microphone wind speed estimates display high frequency variations and resolves short time gusts well. The obtained wind speed estimates can therefore be used to examine turbulence in the PBL, in particular in terms of variability. To do so we must consider a statistic to quantify turbulence within a time series. Gustiness is one such measure of turbulent intensity which characterises the level to which a flow is turbulent. The gustiness metric is given as

$$Gustiness = \frac{\sigma}{\mu}$$

where σ and μ are the standard deviation and mean of the wind speed signal. This is effectively a measure of the variability of the wind speed time series normalised by the average wind speed, to emphasise where a signal greatly varies compared to the ambient wind speed.

This gustiness metric was calculated on the wind speed estimate produced by the GP prediction over each 167s microphone recording. Figure 6 shows the ambient microphone recordings from across the mission to date where each dot represents a recording at a particular LTST and Ls. The size of the dot is scaled to represent the RMS pressure of the microphone signal and the colour encodes the gustiness of that recording. The derived gustiness values for each recording are available in A. E. Stott (2023). It can be seen that strong signal power (larger size dot representing large RMS pressure), and there-

This article is protected by copyright. All rights reserved.

Author Manuscript

fore strong winds, typically occur throughout the afternoon. However, this is not always coincident with strong gustiness values which tend to occur earlier in the sol from 9-13 LTST. This is consistent with Chide et al. (2022) who demonstrate that sound speed derived thermal fluctuations are greatest at this time. The wind earlier on appears more episodic where there is a mix of small and large signal power recordings. On the other hand, the later wind is more consistently strong with few small dots, low signal recordings indicating lulls, in the mid afternoon period.

6.1 Comparison to vortex rates

Pressure drops are another marker of pressure oscillations. Hueso et al. (2022b) has generated a catalogue of pressure drops >0.3 Pa for the first 415 sols of the mission. These data available in Hueso et al. (2022a). In Figure 7 (a) we show a histogram for the number of pressure drops detected within each LTST hour compared to each gustiness value calculated on the microphone wind speed estimate. The pressure drop rates are generally low during the night time and pick up from 10 LTST, peaking at noon and dying down after 17 LTST. The overall distribution of gustiness is a close match to the pressure drop rates but the gustiness has slightly heavier tails over a broader range, increasing from the nighttime lows around 7 LTST and dying off at 18 LTST. There is a recording indicating a relatively high turbulent intensity (with gustiness value around 0.17) just after midnight. This corresponds to a period of nocturnal turbulence, which would be shear driven. This has been observed in MEDA measurements over the mission and is reported in Pla-García et al. (2022).

As mentioned the 167 s length is too short to necessarily be a robust representation of the period. However, the distribution of these values over a time period indicates the variation of the episodic gusts. To that end, Figure 7 (c) quantifies the distribution of gustiness from the microphone for four hour periods over the sol. This shows a violin plot of the wind speed gustiness. Each violin within a violin plot shows the PDF (estimated using a KDE) of gustiness along the y-axis while the x-axis represents the time period of data within each violin. Figure 7 (b) instead shows the distribution of the logarithm of the pressure drops size for the same four hour periods. Within each violin a horizontal line represents an individual observation, indicating the relative lack of observations for the microphone compared to the ability of the continuous measurements of pressure to assess the pressure drop rate. Despite this, similarities can be observed between the distributions particularly during the day time. This comparison verifies that the high frequency wind estimates from the microphone data are suitable to assess turbulence, particularly at small scales.

6.2 Thermal correlations with gustiness

Buoyancy generated turbulence occurs due to atmospheric instability from thermal imbalances. To that end, the correlation of the gustiness metric with the various temperature data recorded by Perseverance is of interest to examine the behaviour and control of turbulence in the PBL. Figure 8 shows scatter plots of the gustiness metric for the microphone-based wind speed against (a) the ground - air temperature difference (gradient), (b) air temperature, (c) the ground temperature, (d) turbulent heat flux, (e) the downwelling atmospheric IR flux and (f) the MEDA wind speed. Each plot shows some level of positive correlation, albeit with a large scatter/variance. It is important to note that these factors are somewhat degenerate, which makes establishing the dominant effect difficult.

The temperature difference between the air and ground is an indication of atmospheric instability. This implies that higher temperature gradients (in particular when the ground is warmer than the air) should generate more intense turbulence. Figure 8 (a) does show that larger gradients do tend to have higher gustiness, although with sig-

This article is protected by copyright. All rights reserved.

Author Manuscript

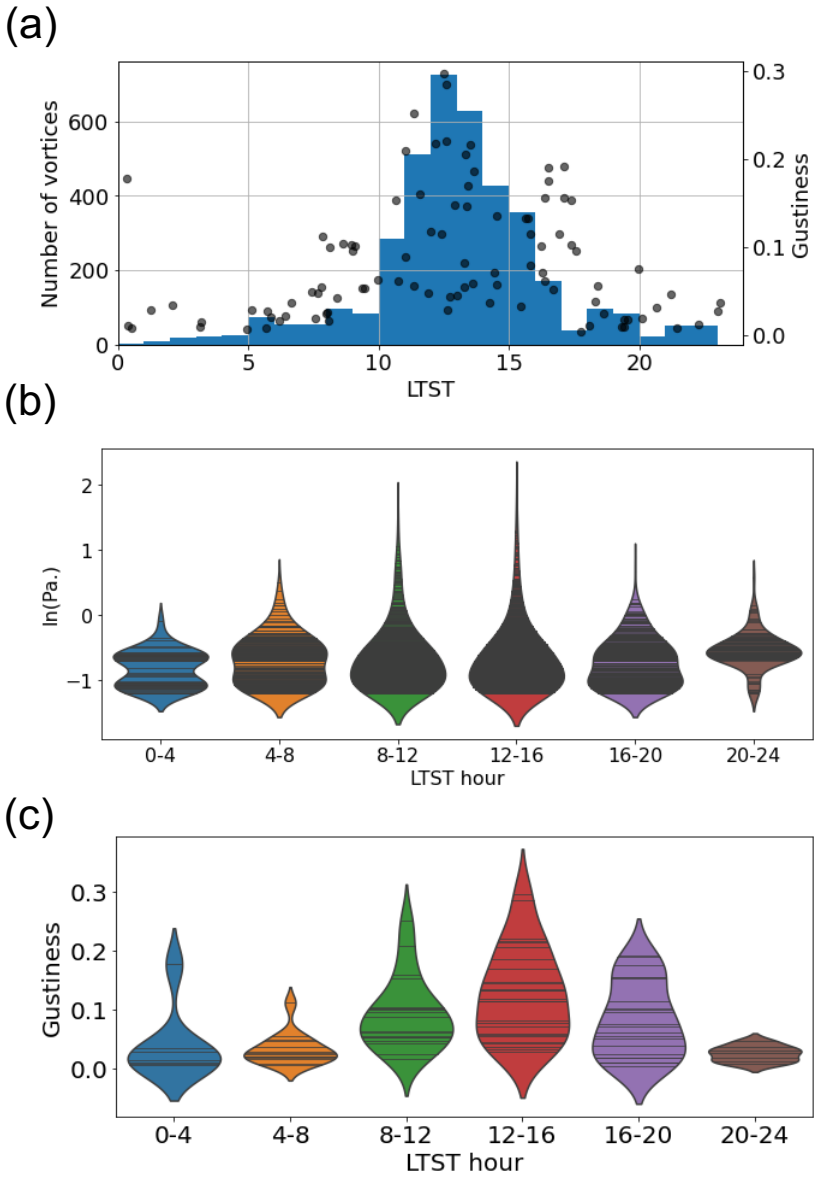


Figure 7. (a) histogram of number of pressure drops >0.3 Pa with a bin for each LTST hour and the gustiness value of each 167s microphone recording at the LTST it occured. (b) violin plot of pressure drops (in terms of ln(Pa)) for four LTST hour groups. (c) violin plot of gustiness for four LTST hour groups.

This article is protected by copyright. All rights reserved.

Author Manuscript

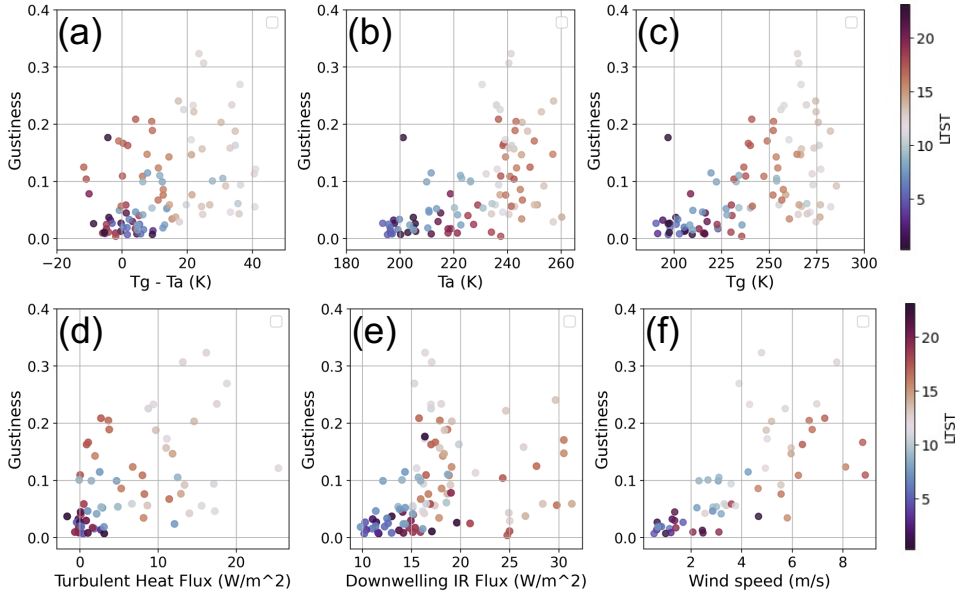


Figure 8. Scatter plots of the relationship between the gustiness statistic derived from the microphone-based GP wind speed prediction against (a) Tg - Ta, (b) Ta and (c) Tg, (d) turbulent heat flux, (e) downwelling IR flux and (f) MEDA wind speed.

nificant (and increasing) variance. Munguira et al. (2023) and De la Torre Juárez and et al. (2022) report a correlation between atmospheric temperature standard deviation (indicating turbulence) and this gradient, thus, in agreement with our findings. They demonstrate a relatively strong correlation during the unstable part of the sol and a weaker reversed correlation for more stable conditions. The microphone gustiness also demonstrates evidence of a separate cluster for the stable periods, shown in Figure 8 (a) by the darker coloured points (nighttime, early morning or late afternoon LTSTs) with low gustiness values where there is nearly no temperature difference between the ground and air.

The overall variation of the PBL is predominantly driven by radiative flux which raises the ground temperature. This drives the instability (thermal gradient) in the PBL giving rise to buoyancy driven turbulence. Spiga et al. (2021) demonstrated that ground temperature is indeed the best explanatory variable for wind gustiness at InSight, verifying the radiative control. We also find a positive correlation, shown in Figure 8 (c), in agreement with these findings. The correlation to ground temperature has an increasing variance with increasing ground temperature, that is, it is heteroscedastic. A similar observation can also be made in Figure 12 of Spiga et al. (2021). This increasing variance with the independent variable (heteroscedasticity) also occurs in the correlations with each of the other variables.

The correlation with air temperature is shown in Figure 8 (b), showing similar features to the other variables. Notice that the nocturnal turbulence (black dot with gustiness = 0.17) appears as an outlier compared to both the relationships with ground and atmospheric temperature, in agreement with it being due to shear rather than buoyancy.

As mentioned, the analysis of Spiga et al. (2021) was performed on averages between 11-14 LTST over the Martian seasons. On the other hand, our analysis is for shorter 167 s signals taken from across the entire sol and over seasons. As a result, we cannot straightforwardly decouple diurnal and seasonal factors. This is highlighted by comparing our correlation to turbulent heat flux (in Figure 8 (d)) to that in Spiga et al. (2021).

This article is protected by copyright. All rights reserved.

Author Manuscript

We show a general increase in gustiness with turbulent heat flux (most clearly for < 5 W/m^2) but Spiga et al. (2021) show a negative correlation. As their analysis is produced for the seasonal evolution of the daytime (11-14 LTST) PBL the range of turbulent heat flux examined is 12-33 W/m^2, while we only show a few points in this range. Above $\sim$ 10 W/m^2, Figure 8 (d) does not in fact show clear correlation, while the majority of points below 10 W/m^2 with a more positive correlation are later afternoon to early morning, outside the period examined by Spiga et al. (2021).

Figure 8 (e) displays the relationship between gustiness and the downwelling atmospheric IR flux, which demonstrates a generally positive correlation. In particular, there is a fairly sharp increase for values 15-20 W/m^2. There are a few recordings with flux above 20 W/m^2 with a wide range of corresponding gustiness. Notice that the recording corresponding to a period of nocturnal turbulence (the black dot with gustiness around 0.17) appears inline with this relationship rather than as an outlier as was the case with atmospheric temperature in Figure 8 (b).

Figure 8 (f) shows a positive correlation between the MEDA wind speed and the microphone-based gustiness. Although this shows an apparent positive correlation, high wind speeds have been posited to inhibit turbulence. There is some indication that noon values (lighter dots) have large turbulent intensity at lower winds speeds, while the late afternoon (red dots) show weaker gustiness for the larger values of wind speed. However, there are not enough data points to draw this conclusion. Moreover, we only observe mean wind speeds up to 10 m/s and so may not observe this effect clearly.

7 Discussion

We have shown that there is a good correlation between the microphone signal level and the wind speed, which can be approximated with a fourth order power law above $\sim$2 m/s. The air temperature allows the model to take into account the diurnal variation of the winds. These relationships enable the prediction of a wind speed using GP regression. The GP calibration yields a suitable method, as it acts to interpolate the observed relationships between the microphone and wind data. This allows the output to exhibit the high frequency variation observed by the microphone rather than trying to overly fit and reproduce the MEDA wind speed retrieval. The non-parametric form of the GP model allows for variation in the calibration function to be taken into account, not strictly confining to the form of a power law which is only shown to work in general. Moreover, the GP incorporates the additional information provided by the air temperature with the microphone data to improve the prediction of wind speeds, particularly with respect to the average wind level. The confidence intervals give an intrinsic understanding of the quality of the wind speed estimation.

From the comparison of the MEDA and microphone-based wind speed time series, we demonstrate that the microphone yields sharp fluctuations on shorter time scales than possible for the MEDA wind speed sampling and therefore, information on high frequency variation in the Martian atmosphere. This follows from the sensitivity analysis and prior works where the microphone is more sensitive to the turbulent fluctuations, u, and so the derived wind estimate is most suitable for their analysis at high frequencies. On the other hand, the microphone-based wind speed estimate is less able to track low and slowly varying winds. This shown in Figure 5 (a) where, during the lull, the MEDA wind speed drifts lower than the stable average of the prediction. While the variation of the GP model prediction is largely based on the microphone data, the air temperature does help indicate the average wind level. This highlights a potential future improvement for the model to better account for the longer term variations and incorporate further features from other data sets.

This article is protected by copyright. All rights reserved.

Author Manuscript

The microphone-based estimate reveals episodic gusts on the 1-10 s scales with temporarily high speeds, the distribution of which appears to change over the sol. The gusts are longer and more episodic around noon while they are shorter and more consistent in the later afternoon. Owing to this gust resolving feature, the microphone wind speed estimate can be used to analyse specific signals such as those made by dust devils (Murdoch et al., 2022). Furthermore, the fine gust resolution can be used to examine the distribution of high wind speeds in turbulent conditions. The range of possible winds is well quantified also by the confidence intervals of the GP model. The microphone wind speed estimates can therefore identify periods where particle lofting thresholds could have been broken (Charalambous, McClean, et al., 2021), especially for short periods. Moreover, the distributions help characterise the variability of winds which has been proposed to be a factor in aeolian process activity (Newman et al., 2022).

The high frequency sampling and gust resolving qualities make the microphone wind estimates advantageous to analyse turbulence, whereby we are able to observe the effects of small scale eddies. To that end, we calculated the gustiness metric as a marker of turbulent intensity which was compared to pressure drop rates and other meteorological data recorded by the Perseverance mission. These gustiness values obtained from the microphone wind speed estimates incorporate both diurnal and seasonal effects and also only calculated over a relatively short time period. The short timescales mean that a particular recording may not necessarily be representative of the PBL behaviour at that time, for example, an entire recording could be during a lull in the normally gusty period around noon. However, the distribution of gustiness values can help characterise the episodic nature, indicating how frequently there can be lulls or high gusts. Recall also that Perseverance moves over ground with varying thermal inertia and albedo, which in turn affects the ground temperature value. The impact of this on the wind field would be an average over the area, making the recorded temperature value perhaps not representative either. These factors each add to the large variance demonstrated by the correlations and prohibit a statistically robust determination of the driving factors, an already difficult task given the complexity of the stochastic system and where many of the variables are correlated to each other.

Nevertheless, the correlations do represent a useful snapshot of PBL activity. Our main observations in relation to turbulent intensity then are:

1. The gustiness values are distributed over the sol similarly to pressure drops in terms of rates and sizes.
2. The gustiness is positively correlated with ground temperature, consistent with the radiative forcing of the PBL and conclusions of Spiga et al. (2021).
3. Observations 1 and 2 verify that the gustiness values obtained from the high frequency microphone wind speed estimates are reasonable estimates of turbulent intensity.
4. The gustiness values tend to increase for an increase in the ground - air temperature gradient, indicating the effect of day time atmospheric instability and convection.
5. There is a positive correlation between the gustiness and wind speed and air temperature and a more complex increase for the lower range of turbulent heat flux.
6. The relationships all show a heteroscedastic variance (an increasing variance with the variable). This is in part due to the short period over which the statistic is evaluated but it helps to characterise the variability at these scales, also captured in the distributional analysis in Figure 7.
7. We observe a nocturnal turbulence (studied for Perseverance in Pla-García et al. (2022)) recording which does not fit to the relationships with temperature (it is not convective turbulence) but is consistent with the relationship to downwelling IR flux.

This article is protected by copyright. All rights reserved.

Author Manuscript

Future work would entail a joint analysis with the more continuously sampled MEDA wind, pressure and temperature data. This continuous analysis would provide context to specific microphone observations and aid the uncoupling of diurnal and seasonal variation. This is demonstrated in Figure 7 where the distributions of the gustiness metric show links with the more complete pressure drop data, while indicating the current lack of density in microphone recordings.

8 Conclusion

This paper provides high frequency wind estimates from Mars using the SuperCam microphone on Perseverance. This is based on the observed relationship between the microphone SPL and the MEDA wind speed, which is shown to correlate well. Additional information is provided by the air temperature, which helps with the diurnal variation and steadier wind speeds the microphone is less sensitive to. The relationships with wind speed, air/ground temperature and pressure well describe the variation in the microphone data. The GP regression model then provides a suitable wind speed estimate and takes into account the associated uncertainty. The derived wind speed estimates produce a consistent analysis with other Mars wind speed data sets but also indicate differences in the characteristics of the fast fluctuations.

This work represents a first analysis of high frequency wind speeds retrieved from a microphone on Mars. To that end, the correlations of gustiness with various meteorological data provides a statistical characterisation of turbulent intensity in the Martian PBL. This can be used to compare to existing PBL models. Future work with a larger data set is required to extract particular features of the high frequency winds, towards defining the behaviour of the dissipative regime on Mars.

Acknowledgments

We are grateful to the many people who helped with this project (in addition to the co-authors) including hardware and operations teams. A. E. Stott acknowledges funding from the CNES postdoctoral fellowship. In France, this project is conducted under the authority of CNES. Part of this research was carried out at the Jet Propulsion Laboratory, California Institute of Technology, under a contract with the National Aeronautics and Space Administration (80NM0018D0004). The US-based coauthors, acknowledge sponsorship from NASA's Mars 2020 project, the Game Changing Development program within the Space Technology Mission Directorate and from the Human Exploration and Operations Directorate. The UPV/EHU team (Spain) is supported by Grant PID2019-109467GB-I00 funded by 1042 MCIN/AEI/10.13039/501100011033/ and by Grupos Gobierno Vasco IT1742-22.

Data Availability

All Mars 2020 raw MEDA data necessary to reproduce each figure shown in this manuscript are available via the Planetary Data System (PDS) Atmospheres node (J. A. Rodriguez-Manfredi & de la Torre Juarez, 2021). All raw acoustic data are publicly available at the Planetary Data System Geosciences Node (Wiens & Maurice, 2021). Derived data used in this work includes a dust devil catalogue (Hueso et al., 2022a), the turbulent heat flux (Martinez, 2022) and the downwelling solar flux (Smith, 2022). All data used in this work is available in (A. E. Stott, 2023) along with code written in Python.

References

Balme, M., & Greeley, R. (2006). Dust devils on earth and mars. *Reviews of Geo-*

This article is protected by copyright. All rights reserved.

Author Manuscript

physics, *44*(3).

Banfield, D., Rodriguez-Manfredi, J., Russell, C., Rowe, K., Leneman, D., Lai, H., ... et al. (2019). Insight auxiliary payload sensor suite (apss). *Space Science Reviews*, *215*(1), 1–33.

Banfield, D., Spiga, A., Newman, C., Forget, F., Lemmon, M., Lorenz, R., ... et al. (2020). The atmosphere of mars as observed by insight. *Nature Geoscience*, *13*(3), 190–198.

Charalambous, C., McClean, J., Baker, M., Pike, W., Golombek, M., Lemmon, M., ... et al. (2021). Vortex-dominated aeolian activity at insight's landing site, part 1: Multi-instrument observations, analysis, and implications. *Journal of Geophysical Research: Planets*, *126*(6), e2020JE006757.

Charalambous, C., Stott, A. E., Pike, W., McClean, J. B., Warren, T., Spiga, A., ... et al. (2021). A comodulation analysis of atmospheric energy injection into the ground motion at insight, mars. *Journal of Geophysical Research: Planets*, *126*(4), e2020JE006538.

Chatain, A., Spiga, A., Banfield, D., Forget, F., & Murdoch, N. (2021). Seasonal variability of the daytime and nighttime atmospheric turbulence experienced by insight on mars. *Geophysical Research Letters*, *48*(22), e2021GL095453.

Chide, B., Bertrand, T., Lorenz, R. D., Munguira, A., Hueso, R., Sánchez-Lavega, A., ... et al. (2022). Acoustics reveals short-term air temperature fluctuations near mars' surface. *Geophysical Research Letters*, *49*(21), e2022GL100333.

Chide, B., Maurice, S., Cousin, A., Bousquet, B., Mimoun, D., Beyssac, O., ... Wiens, R. C. (2020). Recording laser-induced sparks on mars with the supercam microphone. *Spectrochimica Acta Part B: Atomic Spectroscopy*, *174*, 106000.

Chide, B., Maurice, S., Murdoch, N., Lasue, J., Bousquet, B., Jacob, X., ... et al. (2019). Listening to laser sparks: a link between laser-induced breakdown spectroscopy, acoustic measurements and crater morphology. *Spectrochimica Acta Part B: Atomic Spectroscopy*, *153*, 50–60.

Chide, B., Murdoch, N., Bury, Y., Maurice, S., Jacob, X., Merrison, J. P., ... et al. (2021). Experimental wind characterization with the supercam microphone under a simulated martian atmosphere. *Icarus*, *354*, 114060.

Cook, M. R., Gee, K. L., Transtrum, M. K., Lympany, S. V., & Calton, M. (2021). Automatic classification and reduction of wind noise in spectral data. *JASA Express Letters*, *1*(6), 063602.

De la Torre Juárez, M., & et al. (2022). The diurnal cycle of temperature fluctuations at jezero crater. *JGR: Planets*.

Dundas, C. M., Becerra, P., Byrne, S., Chojnacki, M., Daubar, I. J., Diniega, S., ... et al. (2021). Active mars: A dynamic world. *Journal of Geophysical Research: Planets*, *126*(8), e2021JE006876.

Farley, K. A., Williford, K. H., Stack, K. M., Bhartia, R., Chen, A., de la Torre, M., ... et al. (2020). Mars 2020 mission overview. *Space Science Reviews*, *216*(8), 1–41.

Gómez-Elvira, J., Armiens, C., Carrasco, I., Genzer, M., Gómez, F., Haberle, R., ... et al. (2014). Curiosity's rover environmental monitoring station: Overview of the first 100 sols. *Journal of Geophysical Research: Planets*, *119*(7), 1680–1688.

Gómez-Elvira, J., Armiens, C., Castañer, L., Domínguez, M., Genzer, M., Gómez, F., ... et al. (2012). Rems: The environmental sensor suite for the mars science laboratory rover. *Space science reviews*, *170*(1), 583–640.

GPy. (since 2012). *GPy: A gaussian process framework in python.* `http://github.com/SheffieldML/GPy`.

Hart, C. R., Nykaza, E. T., & White, M. J. (2018). Acoustic inversion for monin-obukhov similarity parameters from wind noise in a convective boundary layer. *The Journal of the Acoustical Society of America*, *144*(3), 1258–1268.

This article is protected by copyright. All rights reserved.

Author Manuscript

Hess, S., Henry, R., Leovy, C. B., Ryan, J., & Tillman, J. E. (1977). Meteorological results from the surface of mars: Viking 1 and 2. *Journal of Geophysical Research*, *82*(28), 4559–4574.

Hueso, R., Newman, C., Río-Gaztelurrutia, T. d., Munguira, A., Sánchez-Lavega, A., Toledo, D., ... et al. (2022a). *Catalog of pressure drops, vortices and dust devils on jezero crater, mars, ls=6-213 plus large eddy simulation movie [dataset].* `https://doi.org/10.5281/zenodo.7315863`.

Hueso, R., Newman, C., Río-Gaztelurrutia, T. d., Munguira, A., Sánchez-Lavega, A., Toledo, D., ... et al. (2022b). Convective vortices and dust devils detected and characterized by mars 2020. *Journal of Geophysical Research: Planets*, e2022JE007516.

Kaimal, J. C., Wyngaard, J., Izumi, Y., & Coté, O. (1972). Spectral characteristics of surface-layer turbulence. *Quarterly Journal of the Royal Meteorological Society*, *98*(417), 563–589.

Kurgansky, M. (2019). On the statistical distribution of pressure drops in convective vortices: Applications to martian dust devils. *Icarus*, *317*, 209–214.

Lemmon, M. T., Smith, M. D., Viudez-Moreiras, D., de la Torre-Juarez, M., Vicente-Retortillo, A., Munguira, A., ... et al. (2022). Dust, sand, and winds within an active martian storm in jezero crater. *Geophysical research letters*, *49*(17), e2022GL100126.

Lighthill, M. J. (1954). On sound generated aerodynamically ii. turbulence as a source of sound. *Proceedings of the Royal Society of London. Series A. Mathematical and Physical Sciences*, *222*(1148), 1–32.

Lorenz, R. D. (2022). Turbulence for extraterrestrial aviation: Gust specification for dragonfly's powered flights. *Planetary and Space Science*, *214*, 105459.

Lorenz, R. D., Spiga, A., Lognonne, P., Plasman, M., Newman, C. E., & Charalambous, C. (2021). The whirlwinds of elysium: A catalog and meteorological characteristics of dust devil vortices observed by insight on mars. *Icarus*, *355*, 114119.

Lyons, G. W., Hart, C. R., & Raspet, R. (2021). As the wind blows: Turbulent noise on outdoor microphones. *Acoustics Today*, *17*(4).

Maki, J., Gruel, D., McKinney, C., Ravine, M., Morales, M., Lee, D., ... et al. (2020). The mars 2020 engineering cameras and microphone on the perseverance rover: A next-generation imaging system for mars exploration. *Space Science Reviews*, *216*(8), 1–48.

Mangold, N., Gupta, S., Gasnault, O., Dromart, G., Tarnas, J., Sholes, S., ... et al. (2021). Perseverance rover reveals an ancient delta-lake system and flood deposits at jezero crater, mars. *Science*, *374*(6568), 711–717.

Martinez, G. (2022). *Downwelling LW flux and aerosol opacity at Jezero Crater, Mars, as derived from MEDA/TIRS [Dataset].* `https://repository.hou.usra.edu/handle/20.500.11753/1839`.

Martínez, G., Sebastián, E., Vicente-Retortillo, A., Smith, M. D., Johnson, J. R., Fischer, E., ... et al. (2022). Surface energy budget, albedo and thermal inertia at jezero crater, mars, as observed from the mars 2020 meda instrument. *Journal of Geophysical Research: Planets*, e2022JE007537.

Maurice, S., Chide, B., Murdoch, N., Lorenz, R. D., Mimoun, D., Wiens, R. C., ... et al. (2022). In situ recording of mars soundscape. *Nature*, *605*(7911), 653–658.

Maurice, S., Wiens, R. C., Bernardi, P., Caïs, P., Robinson, S., Nelson, T., ... et al. (2021). The supercam instrument suite on the mars 2020 rover: Science objectives and mast-unit description. *Space Science Reviews*, *217*(3), 1–108.

Mimoun, D., Cadu, A., Murdoch, N., Chide, B., Sournac, A., Parot, Y., ... et al. (2023). The mars microphone onboard supercam. *Space Science Reviews*, *219*(1), 5.

Monin, A., Sergeevich, & Yaglom, A. M. (2013). *Statistical fluid mechanics, volume*

This article is protected by copyright. All rights reserved.

Author Manuscript

ii: mechanics of turbulence (Vol. 2). Courier Corporation.

Morgan, S., & Raspet, R. (1992). Investigation of the mechanisms of low-frequency wind noise generation outdoors. *The Journal of the Acoustical Society of America*, *92*(2), 1180–1183.

Munguira, A., Hueso, R., Sánchez-Lavega, A., Torre-Juarez, M. d. l., Martínez, G., Newman, C., ... et al. (2023). Near surface atmospheric temperatures at jezero from mars 2020 meda measurements. *Journal of Geophysical Research: Planets*, e2022JE007559.

Murdoch, N., Chide, B., Lasue, J., Cadu, A., Sournac, A., Bassas-Portús, M., ... et al. (2019). Laser-induced breakdown spectroscopy acoustic testing of the mars 2020 microphone. *Planetary and Space Science*, *165*, 260–271.

Murdoch, N., Stott, A., Gillier, M., Hueso, R., Lemmon, M., Martinez, G., ... et al. (2022). The sound of a martian dust devil. *Nature Communications*, *13*(1), 7505.

Murphy, J., Steakley, K., Balme, M., Deprez, G., Esposito, F., Kahanpää, H., ... et al. (2016). Field measurements of terrestrial and martian dust devils. *Space Science Reviews*, *203*(1), 39–87.

Newman, C. E., Hueso, R., Lemmon, M. T., Munguira, A., Vicente-Retortillo, Á., Apestigue, V., ... et al. (2022). The dynamic atmospheric and aeolian environment of jezero crater, mars. *Science Advances*, *8*(21), eabn3783.

Petrosyan, A., Galperin, B., Larsen, S. E., Lewis, S., Määttänen, A., Read, P., ... et al. (2011). The martian atmospheric boundary layer. *Reviews of Geophysics*, *49*(3).

Pla-García, J., Munguira, A., Newman, C., Bertrand, T., Martinez, G., Hueso, R., ... et al. (2022). Nocturnal turbulence at jezero crater, as determined from meda measurements and modeling. *Authorea Preprints*.

Raspet, R., Webster, J., & Dillion, K. (2006). Framework for wind noise studies. *The Journal of the Acoustical Society of America*, *119*(2), 834–843.

Raspet, R., Yu, J., & Webster, J. (2008). Low frequency wind noise contributions in measurement microphones. *The Journal of the Acoustical Society of America*, *123*(3), 1260–1269.

Read, P., Galperin, B., Larsen, S. E., Lewis, S. R., Mttnen, A., Petrosyan, A., ... et al. (2017). The martian planetary boundary layer. In R. M. Haberle, R. T. Clancy, F. Forget, M. D. Smith, & R. W. Zurek (Eds.), *The atmosphere and climate of mars* (p. 172202). Cambridge University Press. doi: 10.1017/9781139060172.007

Read, P., Lewis, S., & Mulholland, D. (2015). The physics of martian weather and climate: a review. *Reports on Progress in Physics*, *78*(12), 125901.

Rodriguez-Manfredi, J., de la Torre Juarez, M., Sanchez-Lavega, A., Hueso, R., Martinez, G., Lemmon, M., ... et al. (2023). The diverse meteorology of jezero crater over the first 250 sols of perseverance on mars. *Nature Geoscience*, 1–10.

Rodriguez-Manfredi, J. A., & de la Torre Juarez, M. (2021). *Mars 2020 perseverance rover Mars environmental dynamics analyzer (MEDA) experiment data record (EDR) and reduced data record (RDR) data products archive bundle [Dataset].* `https://doi.org/10.17189/1522849`.

Rodriguez-Manfredi, J. A., De la Torre Juárez, M., Alonso, A., Apéstigue, V., Arruego, I., Atienza, T., ... et al. (2021). The mars environmental dynamics analyzer, meda. a suite of environmental sensors for the mars 2020 mission. *Space science reviews*, *217*(3), 1–86.

Sánchez-Lavega, A., Rio-Gaztelurrutia, T. d., Hueso, R., Juárez, M. d. l. T., Martínez, G., Harri, A.-M., ... et al. (2022). Mars 2020 perseverance rover studies of the martian atmosphere over jezero from pressure measurements. *Journal of Geophysical Research: Planets*, e2022JE007480.

Sebastián, E., Martínez, G., Ramos, M., Haenschke, F., Ferrándiz, R., Fernández,

This article is protected by copyright. All rights reserved.

Author Manuscript

M., & Manfredi, J. A. R. (2020). Radiometric and angular calibration tests for the meda-tirs radiometer onboard nasas mars 2020 mission. *Measurement*, *164*, 107968.

Sebastián, E., Martínez, G., Ramos, M., Perez-Grande, I., Sobrado, J., & Manfredi, J. A. R. (2021). Thermal calibration of the meda-tirs radiometer onboard nasa's perseverance rover. *Acta Astronautica*, *182*, 144–159.

Smith, M. D. (2022). *Perseverance MEDA/TIRS aerosol retrievals [Dataset].* https://doi.org/10.17632/48phhtkcj8.1.

Smith, M. D., Martínez, G. M., Sebastián, E., Lemmon, M. T., Wolff, M. J., Apéstigue, V., ... et al. (2023). Diurnal and seasonal variations of aerosol optical depth observed by meda/tirs at jezero crater, mars. *Journal of Geophysical Research: Planets*, e2022JE007560.

Spiga, A. (2019). The planetary boundary layer of mars. In *Oxford research encyclopedia of planetary science*.

Spiga, A., Murdoch, N., Lorenz, R., Forget, F., Newman, C., Rodriguez, S., ... et al. (2021). A study of daytime convective vortices and turbulence in the martian planetary boundary layer based on half-a-year of insight atmospheric measurements and large-eddy simulations. *Journal of Geophysical Research: Planets*, *126*(1), e2020JE006511.

Stott, A., Garcia, R., Chédozeau, A., Spiga, A., Murdoch, N., Pinot, B., ... et al. (2023). Machine learning and marsquakes: a tool to predict atmospheric-seismic noise for the nasa insight mission. *Geophysical Journal International*, *233*(2), 978–998.

Stott, A. E. (2023). *Perseverance SuperCam microphone wind speeds and gustiness catalogue [Dataset].* https://doi.org/10.5281/zenodo.7863219.

Strasberg, M. (1988). Dimensional analysis of windscreen noise. *The Journal of the Acoustical Society of America*, *83*(2), 544–548.

Stull, R. B. (1988). *An introduction to boundary layer meteorology*.

Temel, O., Senel, C. B., Spiga, A., Murdoch, N., Banfield, D., & Karatekin, O. (2022). Spectral analysis of the martian atmospheric turbulence: Insight observations. *Geophysical Research Letters*, e2022GL099388.

Van den Berg, G. (2006). Wind-induced noise in a screened microphone. *The Journal of the Acoustical Society of America*, *119*(2), 824–833.

Viúdez-Moreiras, D., Gómez-Elvira, J., Newman, C., Navarro, S., Marin, M., Torres, J., ... et al. (2019a). Gale surface wind characterization based on the mars science laboratory rems dataset. part ii: Wind probability distributions. *Icarus*, *319*, 645–656.

Viúdez-Moreiras, D., Gómez-Elvira, J., Newman, C., Navarro, S., Marin, M., Torres, J., ... et al. (2019b). Gale surface wind characterization based on the mars science laboratory rems dataset. part i: Wind retrieval and gale's wind speeds and directions. *Icarus*, *319*, 909–925.

Viúdez-Moreiras, D., Lemmon, M., Newman, C., Guzewich, S., Mischna, M., Gómez-Elvira, J., ... et al. (2022). Winds at the mars 2020 landing site: 1. near-surface wind patterns at jezero crater. *Journal of Geophysical Research: Planets*, *127*(12), e2022JE007522.

Viúdez-Moreiras, D., Torre, M. d. l., Gómez-Elvira, J., Lorenz, R., Apéstigue, V., Guzewich, S., ... et al. (2022). Winds at the mars 2020 landing site. part 2: Wind variability and turbulence. *Journal of Geophysical Research: Planets*, e2022JE007523.

Wang, H., & Richardson, M. I. (2015). The origin, evolution, and trajectory of large dust storms on mars during mars years 24–30 (1999–2011). *Icarus*, *251*, 112–127.

Wiens, R. C., & Maurice, S. A. (2021). *Mars 2020 Perseverance Rover SuperCam Raw, Calibrated, and Derived Data Products [Dataset].* https://doi.org/10.17189/1522646.

This article is protected by copyright. All rights reserved.

Williams, C., & Rasmussen, C. (1995). Gaussian processes for regression. *Advances in neural information processing systems*, *8*.

Wilson, D. K., Greenfield, R. J., & White, M. J. (2007). Spatial structure of low-frequency wind noise. *The Journal of the Acoustical Society of America*, *122*(6), EL223–EL228.

Wu, Z., Richardson, M. I., Zhang, X., Cui, J., Heavens, N. G., Lee, C., ... et al. (2021). Large eddy simulations of the dusty martian convective boundary layer with marswrf. *Journal of Geophysical Research: Planets*, *126*(9), e2020JE006752.

Zurek, R. W., & Martin, L. J. (1993). Interannual variability of planet-encircling dust storms on mars. *Journal of Geophysical Research: Planets*, *98*(E2), 3247–3259.

Author Manuscript

This article is protected by copyright. All rights reserved.